Characterization of light collection through a subwavelength aperture from a point source

Xin Heng[1], Xiquan Cui[1], David W. Knapp[2], Jigang Wu[1], Zahid Yaqoob[1], Emily J. McDowell[3], Demetri Psaltis[1], and Changhuei Yang[1,3]

[1]Department of Electrical Engineering (MC136-93), [2]Division of Chemistry and Chemical Engineering (MC127-72), [3]Department of Bioengineering (MC138-78), California Institute of Technology, Pasadena, CA, 91125
xin@caltech.edu

Abstract: We experimentally measure and theoretically model the light transmission characteristics of subwavelength apertures. The characterization consists of translating a point source at varying vertical height and lateral displacement from the aperture and measuring the resulting transmission. We define the variation of the transmission with lateral source displacement as the collection mode point spread function (CPSF). This transmission geometry is particularly relevant to subwavelength aperture based imaging devices and enables determination of their resolution. This study shows that the achieved resolutions degrade as a function of sample height and that the behavior of sensor devices based on the use of apertures for detection is different from those devices where the apertures are used as light sources. In addition, we find that the measured CPSF is dependent on the collection numerical aperture (NA). Finally, we establish that resolution beyond the diffraction limit for a nominal optical wavelength of 650 nm and nominal medium refractive index of 1.5 is achievable with subwavelength aperture based devices when the aperture size is smaller than 225 nm.

OCIS codes: (110.1220) Apertures; (170.5810) Scanning microscopy; (130.0130) Integrated optics

References and links

1. E. Popov, M. Neviere, P. Boyer and N. Bonod, "Light transmission through a subwavelength hole," Opt. Commun. **255**, 338-348, (2005).
2. E. X. Jin and X. F. Xu, "Obtaining super resolution light spot using surface plasmon assisted sharp ridge nanoaperture," Appl. Phys. Lett. **86**, (2005).
3. X. L. Shi, L. Hesselink and R. L. Thornton, "Ultrahigh light transmission through a C-shaped nanoaperture," Opt. Lett. **28**, 1320-1322, (2003).
4. H. J. Lezec, A. Degiron, E. Devaux, R. A. Linke, L. Martin-Moreno, F. J. Garcia-Vidal and T. W. Ebbesen, "Beaming light from a subwavelength aperture," Science **297**, 820-822, (2002).
5. H. J. Lezec and T. Thio, "Diffracted evanescent wave model for enhanced and suppressed optical transmission through subwavelength hole arrays," Opt. Express **12**, 3629-3651, (2004).
6. T. W. Ebbesen, H. J. Lezec, H. F. Ghaemi, T. Thio and P. A. Wolff, "Extraordinary optical transmission through sub-wavelength hole arrays," Nature **391**, 667-669, (1998).
7. M. J. Levene, J. Korlach, S. W. Turner, M. Foquet, H. G. Craighead and W. W. Webb, "Zero-mode waveguides for single-molecule analysis at high concentrations," Science **299**, 682-686, (2003).
8. J. Wenger, P. F. Lenne, E. Popov, H. Rigneault, J. Dintinger and T. W. Ebbesen, "Single molecule fluorescence in rectangular nano-apertures," Opt. Express **13**, 7035-7044, (2005).
9. A. G. Brolo, R. Gordon, B. Leathem and K. L. Kavanagh, "Surface plasmon sensor based on the enhanced light transmission through arrays of nanoholes in gold films," Langmuir **20**, 4813-4815, (2004).
10. A. Partovi, D. Peale, M. Wuttig, C. A. Murray, G. Zydzik, L. Hopkins, K. Baldwin, W. S. Hobson, J. Wynn, J. Lopata, L. Dhar, R. Chichester and J. H. J. Yeh, "High-power laser light source for near-field optics and its application to high-density optical data storage," Appl. Phys. Lett. **75**, 1515-1517, (1999).
11. F. Chen, A. Itagi, J. A. Bain, D. D. Stancil, T. E. Schlesinger, L. Stebounova, G. C. Walker and B. B. Akhremitchev, "Imaging of optical field confinement in ridge waveguides fabricated on very-small-aperture laser," Appl. Phys. Lett. **83**, 3245-3247, (2003).

#74321 - $15.00 USD Received 22 August 2006; revised 18 October 2006; accepted 20 October 2006

12. A. Sundaramurthy, P. J. Schuck, N. R. Conley, D. P. Fromm, G. S. Kino and W. E. Moerner, "Toward nanometer-scale optical photolithography: Utilizing the near-field of bowtie optical nanoantennas," Nano Lett. **6**, 355-360, (2006).
13. J. O. Tegenfeldt, O. Bakajin, C. F. Chou, S. S. Chan, R. Austin, W. Fann, L. Liou, E. Chan, T. Duke and E. C. Cox, "Near-field scanner for moving molecules," Phys. Rev. Lett. **86**, 1378-1381, (2001).
14. X. Heng, D. Erickson, L. R. Baugh, Z. Yaqoob, P. W. Sternberg, D. Psaltis and C. Yang, "Optofluidic microscopy- a method for implementing a high resolution optical microscope on a chip," Lab on a Chip **6**, 1274 - 1276, (2006).
15. T. R. Corle and G. S. Kino, *Confocal scanning optical microscopy and related imaging systems*, San Diego: Academic Press, 1996.
16. M. G. L. Gustafsson, "Nonlinear structured-illumination microscopy: Wide-field fluorescence imaging with theoretically unlimited resolution," Proceedings of the National Academy of Sciences of the United States of America **102**, 13081-13086, (2005).
17. S. W. Hell and J. Wichmann, "Breaking the Diffraction Resolution Limit by Stimulated-Emission - Stimulated-Emission-Depletion Fluorescence Microscopy," Opt. Lett. **19**, 780-782, (1994).
18. D. P. Tsai, A. Othonos, M. Moskovits and D. Uttamchandani, "Raman-Spectroscopy Using a Fiber Optic Probe with Subwavelength Aperture," Appl. Phys. Lett. **64**, 1768-1770, (1994).
19. K. Okamoto and S. Kawata, "Radiation force exerted on subwavelength particles near a nanoaperture," Phys. Rev. Lett. **83**, 4534-4537, (1999).
20. E. Betzig, J. K. Trautman, T. D. Harris, J. S. Weiner and R. L. Kostelak, "Breaking the Diffraction Barrier - Optical Microscopy on a Nanometric Scale," Science **251**, 1468-1470, (1991).
21. D. Courjon, *Near-field microscopy and near-field optics*, London: Imperial College Press, 2003.
22. S. Inoue and K. R. Spring, *Video microscopy: the fundamentals*, (2nd edition, New York : Plenum Press, 1997).
23. J. W. Goodman, *Introduction to Fourier optics*, (3rd edition, New York : McGraw-Hill, 2004).
24. L. G. Schulz and F. R. Tangherlini, "Optical Constants of Silver, Gold, Copper, and Aluminum .2. the Index of Refraction-N," J. Opt. Soc. Am. **44**, 362-368, (1954).
25. L. G. Schulz, "The Optical Constants of Silver, Gold, Copper, and Aluminum .1. the Absorption Coefficient-K," J. Opt. Soc. Am. **44**, 357-362, (1954).
26. E. Grupp, H. J. Lezec, T. Thio and T. W. Ebbesen, "Beyond the Bethe limit: Tunable enhanced light transmission through a single sub-wavelength aperture," Adv. Mater. **11**, 860-862, (1999).
27. COMSOL Multiphysics 3.2 (2006), *COMSOL Inc*. (http://www.comsol.com/).
28. N. N. Rao, *Elements of engineering electromagnetics* (6th edition, Upper Saddle River, N.J. : Pearson Prentice Hall, 2004.
29. J. P. Berenger, "Three-dimensional perfectly matched layer for the absorption of electromagnetic waves," J. Comp. Phys. **127**, 363-379, (1996).
30. J. Jin, *The finite element method in electromagnetics* (2nd edition, New York: Wiley, 2002.
31. F. Collino and P. Monk, "The perfectly matched layer in curvilinear coordinates," SIAM Journal on Scientific Computing **19**, 2061-2090, (1998).
32. S. D. Gedney, "An anisotropic perfectly matched layer-absorbing medium for the truncation of FDTD lattices," IEEE Trans. Antennas Propag. **44**, 1630-1639, (1996).

1. Introduction

Subwavelength apertures are known to possess interesting characteristics. The unique transmission and diffraction properties of a subwavelength circular aperture [1], a single nanoaperture with designed shapes [2, 3], a single nanoaperture surrounded by corrugated surface [4] or a tightly-spaced nanoaperture array [5, 6] have all been studied and reported in the recent past. While the transmission properties of subwavelength apertures are yet to be fully understood from the theoretical standpoint, subwavelength apertures have been used to demonstrate some remarkable improvements in areas such as bio-molecule analysis [7, 8], sensing [9], recording & storage [10], laser technology [11], as well as photolithography [12].

In particular, the use of subwavelength apertures for high resolution imaging [13, 14] is of significant interest. Subwavelength aperture based imaging devices (ABIDs) have the potential to deliver resolution that is beyond the diffraction limit; the resolution of such devices is fundamentally limited by the aperture size. In addition, these devices have the distinct advantage of enabling compact and portable analysis systems. As such, ABID compares favorably with imaging systems based on other optical imaging strategies, such as laser scanning confocal microscopy [15], structured illumination [16] and stimulated emission depletion microscopy [17].

#74321 - $15.00 USD Received 22 August 2006; revised 18 October 2006; accepted 20 October 2006

In general, there are two categories of ABIDs: in one, the apertures are the illumination sources (type-I ABIDs, Fig. 1(a)); in the other, the apertures are the collection units (type-II ABIDs, Fig. 1(b)). The device developed by Tegenfeldt, *et al*. [13] is a type I device. In that device, a nanoslit trio was used to map the length of extended DNA molecules within a nanofluidic chip. The nanoslits functioned as near field illumination sources, and a resolution of 200 nm was reported when the device was used to image fluorescent beads. More recently, our group reported the use of apertures as parallel light collectors to record a transmission image of an object as it is transported within a microfluidic chip – this imaging system, which we name the optofluidic microscope (OFM) [14], is a type II ABID device.

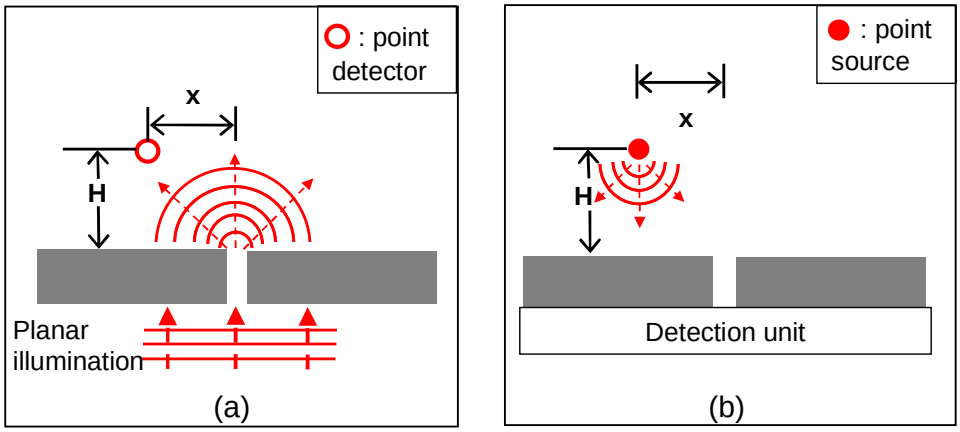

Fig. 1. Two schemes of subwavelength aperture based imaging devices (ABIDs): (a) type-I, (b) type-II. H: vertical separation of point from aperture. x: the lateral displacement of point detector/source from the aperture.

The optical geometry for Type I ABIDs is straightforward. A planar illumination onto the aperture results in a specific transmission and diffraction pattern of the near and far field components on the exit side of the aperture (see Fig. 1(a)). The associated diffraction pattern is directly related to the resolution of type-I ABIDs. To our knowledge, almost all of the publications to date that have investigated light transmission through apertures[1-6], employed this geometry or other closely related geometries.

Unfortunately, this geometry is not suitable for characterizing type-II ABIDs. The performance of a type-II ABID should be studied with a point source that is located at varying height (H) and lateral displacement (x) from the aperture (see Fig. 1(b)). While the optical geometries of type-I and type-II ABIDs may appear to be complements of each other by optical reversibility, in reality, they can behave quite differently. The two would indeed be optical complements under the condition that the detection unit in Fig. 1(b) is sensitive only to the plane wave component of the transmitted light that exits the aperture in the normal incidence direction (an exact complement to the incident plane wave in Fig. 1(a)). However, a realistic detection unit is sensitive to the total power flux and is indiscriminate of the light field wavefront; this breaks the required symmetry.

The primary objective of this paper is to theoretically model and experimentally measure the transmission characteristics of a point source at varying height and lateral displacement from a subwavelength aperture (Fig. 1(b)). While our focus is to apply our findings to design better type-II ABIDs, this geometry may also be of relevance to research areas, such as near field Raman scattering [18] and near field radiation force [19]. In Section 2, we will report on our experimental measurements of the collection mode point spread functions (CPSFs) (formally defined in Section 2) for different aperture sizes. In Section 3, we will describe the 3D electromagnetic simulation method that we used to model this optical geometry. In

#74321 - $15.00 USD Received 22 August 2006; revised 18 October 2006; accepted 20 October 2006

Section 4, we will discuss the validation of our simulation method with our experimental data. In the Results and Discussions section (Section 5), we will use our experimental and simulation results to address the following issues: 1). The resolutions of type-II ABIDs and the far field trend. We will also compare type-II ABIDs and type-I ABIDs. 2) The dependency of the CPSF of the aperture on the numerical aperture (NA) of the collection optics. 3) The relationship between aperture size and the CPSF when the point source is close to the aperture, as well as the theoretical resolution limit of a type-II ABID imposed by the aperture size.

2. Experimental method

The geometry shown in Fig. 1(b) can be used for the characterization of the transmission through an aperture from a point object. For clarity, we define the collection mode point spread function (CPSF) as the function of the transmission versus the lateral displacement of an isotropic point source that is scanned over the aperture at a fixed height. This CPSF is analogous to the point spread function (PSF) generally defined for a near field scanning optical microscope (NSOM) [20, 21].

The resolving power of a type-II ABID can be related to the CPSF as follows. Consider two non-interfering point sources of equal strength at the same height above the aperture. The resolution of the type-II ABID is equal to the minimum lateral separation between these two point objects such that the peaks of their CPSFs are sufficiently separated to be distinguishable. One criterion – the Sparrow's limit [15], defines the resolution as the separation between the two point sources to be such that the composite point spread function has a zero second derivative in the center. This criterion does not assume a particular PSF profile and forms a good basis for an unbiased comparison of resolution between systems with different PSF profiles (for example, a conventional microscope's PSF is described by a Bessel function [22, 23], while a type-II ABID's CPSF is not). We will use this criterion in our comparison of type-II ABIDs with conventional microscopes in Section 5.3. To keep our measurements and analysis general, we choose to quantify the CPSFs in the following sections by their full width at half maximum (FWHM) – a quantity that is more widely used for characterizing PSFs as they are easily measured and conceptually simple to understand.

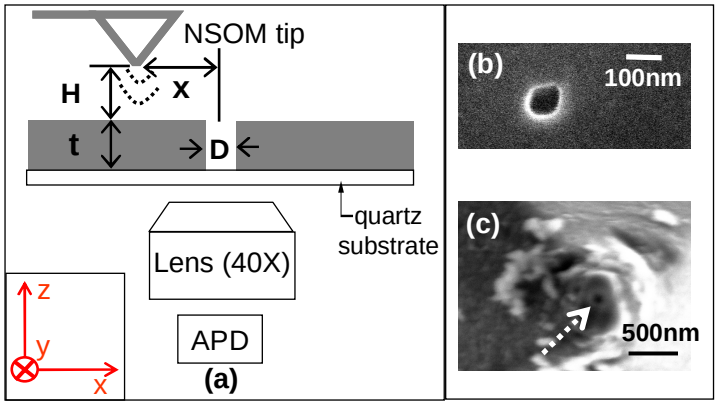

Fig. 2. (a) Illustration of the experimental scheme. The NSOM tip scans over the subwavelength aperture (diameter: D) milled in a thin aluminum film (thickness: t) at a constant height (H). Substrate is an ultra-clean quartz wafer. x: the lateral distance between the NSOM tip and the aperture center. (b) SEM image of a FIB milled aperture; D=100 nm. (c) SEM image of a NSOM tip with a diameter of ~100 nm.

In principle, the experiment should be performed with an ideal point source. In the experiment, an NSOM tip (WITec Gmbh, λ_0= 650 nm) with a 100 nm characteristic diameter (Fig 2(c)) was used as the light source. We approximated the NSOM tip as a point source. The

#74321 - $15.00 USD Received 22 August 2006; revised 18 October 2006; accepted 20 October 2006

impact of the finite tip size and its non-isotropic radiation pattern will be discussed in Section 4. We scanned the NSOM tip at various heights (H) and measured the transmission through the aperture. We characterized the CPSF based on the collected data.

The subwavelength apertures were milled in an aluminum film coated on quartz wafer by using high resolution focused ion beam milling (FEI nova 200 dual-beam FIB). Aluminum was chosen in our experiment, as it is a highly optically absorptive metal. The refractive index of aluminum is given by $n = 1.24 + 6.6 \times i$ at $\lambda_0 = 650$ nm [24, 25], which implies an amplitude-associated skin depth of 15.7 nm. The thickness of the aluminum layer was 60 nm or ~ 4 times the skin depth. The aperture diameter ranged from 100 nm to 1000 nm; the aperture size was measured with a scanning electron microscope (SEM) (Hitachi S4100). The SEM image of an aperture with a diameter of 100 nm is shown in Fig. 2(b). For each diameter value, multiple apertures were created on the metal film with sufficient inter-aperture spacing (more than 20 μm), so that the surface plasmon induced anomalous transmission of the subwavelength apertures did not occur. The apertures were planarized with diluted SU8 resin; this prevented the NSOM tip from dipping into the apertures during scanning.

Our NSOM system was a commercial near field microscope (Alpha-SNOM, WITec Gmbh.). In our experiments, as illustrated in Fig. 2(a), the NSOM tip scanned over the aperture (diameter: D), at a constant height (H) above the metal surface. The illumination through the NSOM tip was provided by a red laser diode ($\lambda_0 = 650$ nm, 30mW). The total transmission through the aperture was collected by a microscope objective (Nikon 40X, NA=0.6) and detected with an avalanche photodiode (AQ series, Perkin Elmer Optoelectronics).

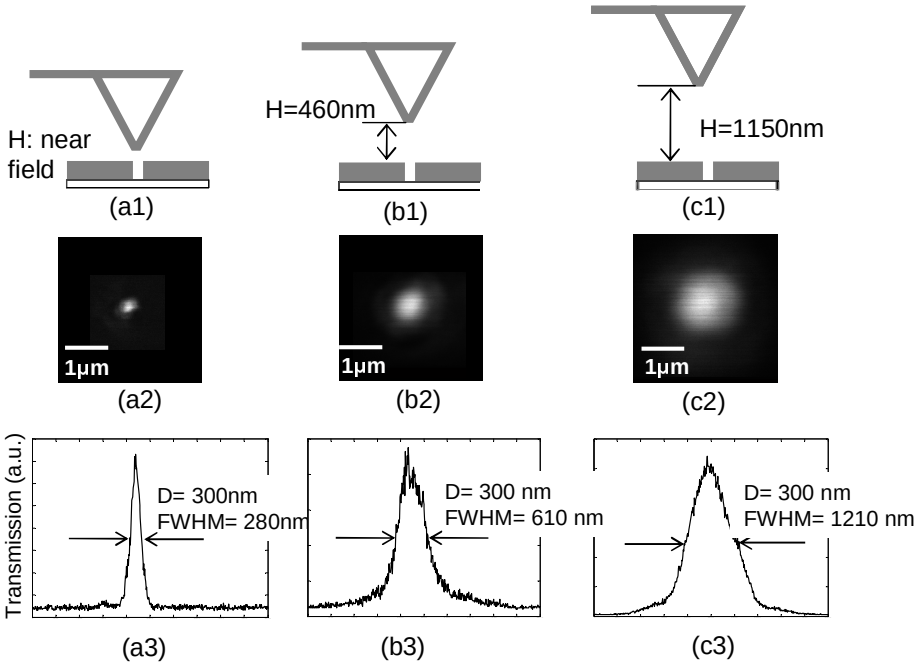

Fig. 3. NSOM measurements of a subwavelength aperture (D= 300 nm). (a1) An illustration of the experimental scheme, with the NSOM tip engaged in the near field; (a2) the collected NSOM image with the experimental geometry shown in (a1); (a3) the CPSF curve extracted from the NSOM image shown in (a2). (b1) - (b3) The corresponding geometry and data with H = 460 nm. (c1) - (c3) The corresponding geometry and data with H = 1150 nm.

As this specific NSOM tool only operates in the contact mode, we used the following method to vary the scan height of the probe tip from the aperture. Thin films of silicon dioxide

#74321 - $15.00 USD Received 22 August 2006; revised 18 October 2006; accepted 20 October 2006

(refractive index = 1.5) of specific thickness were coated on top of the aperture by plasmon enhanced chemical vapor deposition (STS PECVD system) successively. The NSOM tip was scanned across the aperture to collect the CPSF profile between each coating. The accumulative thickness of silicon dioxide was measured by a film thickness measurement tool (SCI FilmTek 2000) after each coating step. This process was repeated until a height of 1.15μm was reached. We note that refractive index of the silicon dioxide layers is accounted for in the simulations described in Sections 3 and 4.

Figure 3 shows an example of our collected NSOM data; the size of aperture in this example is 300 nm. From Fig. 3(a2 → c2) and (a3 → c3), it can be clearly seen that the measured CPSF of the aperture widens as H becomes larger.

The described experiment departs from an ideal point-source experiment in three ways. First, as mentioned above, the NSOM tip was approximated as a point source. The finite NSOM tip size can be expected to cause experimental inaccuracy when used to quantify the CPSFs of small apertures. Second, the radiation dipole components of the tip are largely confined to the x-y plane [26], which is a deviation from an ideal point source where the radiation pattern is isotropic. Finally, the transmission through the aperture is collected with a finite NA objective in the experiment. Ideally, we will like to detect the entire transmitted component. These deviations from an ideal experiment are not the result of flawed experimental design, but are instead due to the practical limitations of existing NSOM technology.

3. Simulation method

In addition to the NSOM walking experiment described in Section 2, we also applied an electromagnetic (EM) simulation scheme to study the same point source scanning geometry. The use of a simulation approach, as opposed to an analytical calculation is necessitated by two facts. First, the finite conductivity of the metal layer needs to be accounted for. Second, we need to model the transmission through the apertures for a range of spatial locations of the point source. The lack of spatial symmetry in most of these situations complicates the analysis.

In this study, the commercial software, COMSOL Multiphysics 3.2 [27], was used. The time averaged power flow (*S*), i.e. Poynting vector, was chosen to quantify the total transmission of the aperture. Hertzian dipole [28] (i.e. a short line source) of length 10 nm (much shorter than the optical wavelength) was adopted in our simulations. In each simulation run, the dipole was placed at a given height (H) and lateral displacement (x) from the aperture (Fig. 4). For each source location, the orientation of the dipole was alternated through three orthogonal orientations – along x-, y- and z-axis in three simulation runs. The combination of the resulting Poynting vector fields for the three runs enabled us to create an isotropic radiation field emanating from that source location – an effective point source. We calculate the total transmission through the aperture as the summation of the transmissions from all three dipole orientations. The parameters of the simulations were chosen to match with those of the experiments. Figures 5(a, c) and Figs. 5(b, d) show examples of the simulation results with the effective point source at different lateral displacement (H= 50 nm, D= 300 nm). As are apparent in the figures, the transmission through the aperture can be significantly altered by varying the lateral position of the light source.

A CPSF can thus be generated by moving the light source across the aperture in the simulation and plotting the transmission as a function of the source's lateral displacement. As illustrated in Fig. 4, the total transmitted power is recorded by a virtual detector located 0.2 μm below the metal surface. Fig. 6(a-c) clearly illustrate the widening trend of the CPSFs with increasing H.

#74321 - $15.00 USD Received 22 August 2006; revised 18 October 2006; accepted 20 October 2006

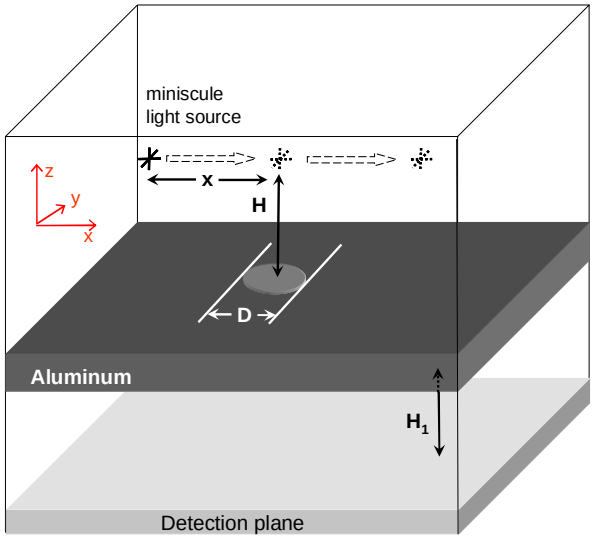

Fig. 4. Schematic of the simulation geometry. The arrows indicate the movement of the light source in the simulation space. The detection plane is 0.2μm underneath the subwavelength aperture. H1 = 0.2μm (distance between metal's bottom surface and the detector plane). D, H and x are defined the same way as those in Fig. 2.

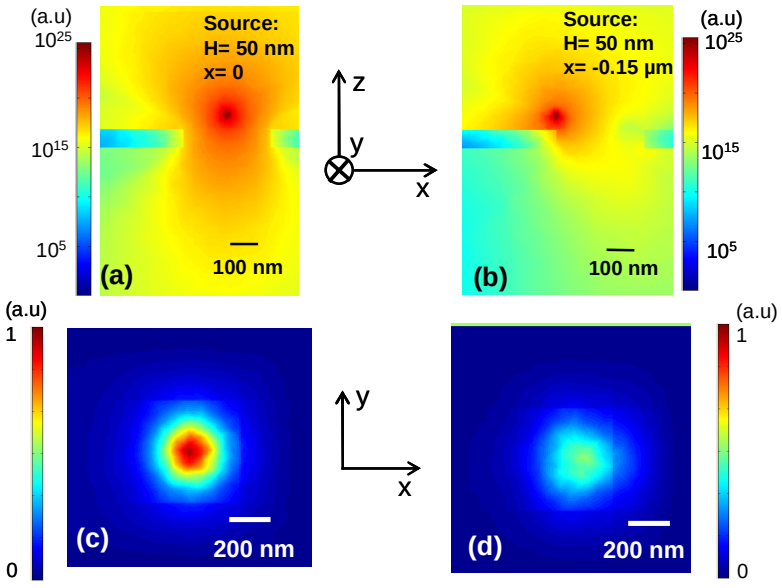

Fig. 5. Examples of the simulation results with all three polarizations considered. (a) Cross sectional plot of power flow (|S|), time averaged; H=50 nm, D= 300 nm, x= 0. (c) Plot of |S| on the detector plane. (b) and (d) show the corresponding plots when x is changed to x = -0.15 μm.

#74321 - $15.00 USD Received 22 August 2006; revised 18 October 2006; accepted 20 October 2006

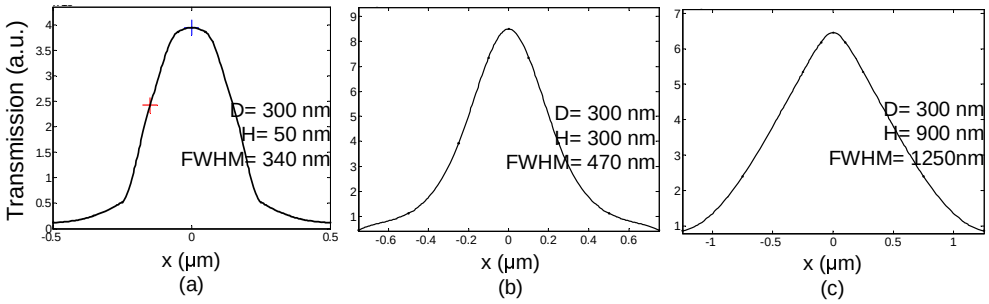

Fig. 6. (a)-(c) Simulation generated CPSF plots for source at different heights from the aperture. The blue cross and the red cross indicate the transmissions corresponding to the point source geometries in Fig. 5(a) and Fig. 5(b), respectively.

The choice of numerical boundaries deserves some discussions. In this software, the outer boundaries that enclose the entire simulation space cause spurious numerical reflections, thus adding errors to simulation results. The low-order scattering boundary conditions provided by the software were not sufficient to suppress the reflection errors. Among all the possible means of solving this problem, perfectly matched layers (PMLs) have been accepted as one of the most effective. As such, we incorporated this scheme into our simulation. However, we note that the numerical reflection on the interface between the constant-value PMLs and the real medium (i.e. SiO_2 in our case), though greatly reduced, still exists because of the finite mesh discretization at this interface [29, 30]. Therefore, a method of variant-PMLs was adopted to truncate the computation domains, with the coordinate stretching factor (a_z) defined as [30]:

$$a_z = 1 - j\left(\frac{z - z_0}{L}\right)^m \delta \tag{1}$$

where z_0 is the z-coordinate of the interface between PML and the glass medium and L is the thickness of PML; m and δ define the absorption property of the PMLs. In x and y directions, a_x and a_y can be similarly defined. In our study, we chose L =0.4 μm, m =2, δ =1, which are consistent with the PML optimization designs of other computational physicists [29-32]. After defining PMLs, we chose an iterative solver, GMRES (generalized minimum residual method) with a geometric multigrid preconditioner to solve the 3D computation problem. The mesh step size was no larger than 100 nm, which resulted in a rapid convergence during the process of iterative computation.

4. Comparison of simulation results and experimental results

As mentioned in Section 2, the experimental limitations are expected to cause systematic errors in the experimentally measured CPSFs. On the other hand, the simulation model requires cross-verifications. In this section, we first compare the experimental and simulation results by adjusting the simulation parameters to match with the experimental conditions. Specifically, we adapt the light source in the simulations to more closely resemble the actual NSOM tip. A comparison of the experimental data and the simulation result serves to validate the simulation model. Finally, we run the simulations based on ideal experimental conditions and compute the CPSFs for a range of aperture sizes and varying point source heights.

We experimentally measured the CPSFs for five aperture sizes: 100 nm, 150 nm, 300nm, 450 nm and 550 nm by using the experimental procedure described in Section 2. The dielectric medium refractive index was 1.5. In our experiments, H ranged from a near field value (≤5 nm) to 1.15 μm. The FWHMs of the measured CPSFs are plotted in Fig. 7 (log-log scale).

#74321 - $15.00 USD Received 22 August 2006; revised 18 October 2006; accepted 20 October 2006

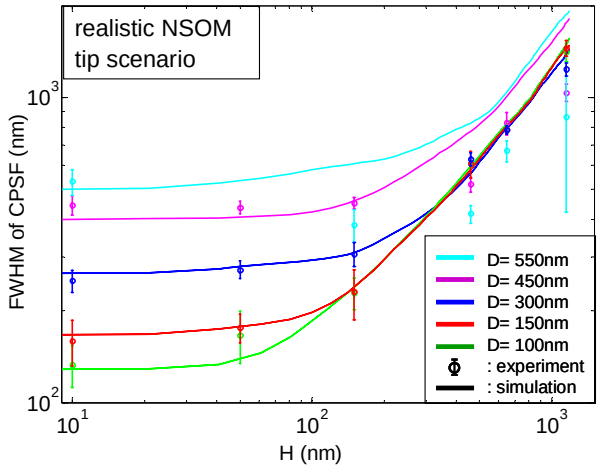

Fig. 7. (log-log scale): CPSF's FWHM *versus* the gap height (H) for a range of aperture sizes (realistic NSOM tip scenario). The lines represent simulation results and the circles represent experimental data. To match with the experimental conditions, only the line sources at lateral directions (i.e. x and y) were considered. The simulation model was adapted to match with the NSOM radiation characteristics. The collection N.A. for the transmission is effectively unity.

The data was fit with the theoretical CPSFs profiles created by using the EM simulation scheme described in Section 3 with the following modifications. First, the point source was simplified into a combination of x- and y- dipole components – to better match the radiation pattern of the NSOM nanoaperture probe [26]. Second, we convolved the probe's aperture function (Gaussian with FWHM of 100 nm) with the simulated CPSFs to generate broadened CPSFs that can account for the finite size of the NSOM tip. The simulation results are plotted in Fig. 7.

The goodness of fit between simulation result and experimental data (see Fig. 7) is excellent for most of the data points. However, the experiment and simulation do deviate significantly for the last three points of the data set for the 450 nm diameter aperture and for most of the data set for the 550 nm diameter aperture, in which the difference is especially large. The measured width of the CPSF for that aperture size actually dipped as a function of H – a counter intuitive behavior.

We believe this discrepancy between simulation and experiment is attributable to the finite collection NA associated with the collection optics in the experiment. In comparison, the simulation uses a geometry that provides nearly perfect collection of the transmitted light. The transmission through a large aperture tends to propagate dominantly along the input light field direction; in comparison, a small aperture diffracts the transmission broadly. Due to the transmission's directionality, a large fraction of the transmitted light will miss the collection optics when the incident angle of the incoming light is large, as in the case where the lateral displacement of the light source is large and the light source is sufficiently distant from the aperture. The drop-off in the collected signal for large lateral displacements leads to an effectively narrower CPSF and lower FWHM value. The observed lower experimentally measured FWHM value is consistent with this explanation (see 450 nm and 550 nm apertures in Fig. 7). We studied the interplay between measured CPSF and the NA of the collection optics more closely in a different set of experiments and an account of our findings is reported in Section 5.2.

With the simulation model validated, we proceeded to compute the CPSFs for apertures of varying sizes based on our model description in Section 3. The FWHMs of the CPSFs are plotted in Fig. 8. We can see that the widths of the CPSFs are at their minimum when H is small; the respective width matches the apertures' size. This corresponds well with our

#74321 - $15.00 USD Received 22 August 2006; revised 18 October 2006; accepted 20 October 2006

expectation that the resolution of type-II ABIDs is determined by the aperture size and that the best resolution is achieved when the aperture is close to the target - a well known property of near field optical imaging.

5. Results and discussions

5.1 The resolution of type-II ABIDs and the far field resolution trends

The plots in Fig. 8 can be used to characterize the resolution in type-II ABID devices. There are a few issues of note. First, as the CPSFs are narrowest when H is small, we can conclude that a type-II ABID should provide highest possible resolution when the target sample is at close proximity to the aperture. For clarity in our nomenclature, we shall refer to this quantity as the resolution limit. Second, we can see in Fig. 8 that as the height (H) of the point source increases, the CPSFs begin to widen. This corresponds to a degradation of the resolution when the target is at a larger distance from the aperture. This height-dependent increase in the CPSFs' widths can be quantified by the depth of field (DOF), a quantity that corresponds to the axial working range of an imaging system. We define the DOF to be the height at which the width of the CPSF is twice that of the CPSF when the height is zero. The DOF values for the apertures are summarized in Table 1. It is worth noting that the aperture size D appears to be a good estimate to the DOF. This implies that, as a rough rule of thumb, to achieve good resolution with type-II ABIDs, the plane of interest in the target object should be maintained at a height (H) above the aperture plane that is no larger than the value of the aperture size (D).

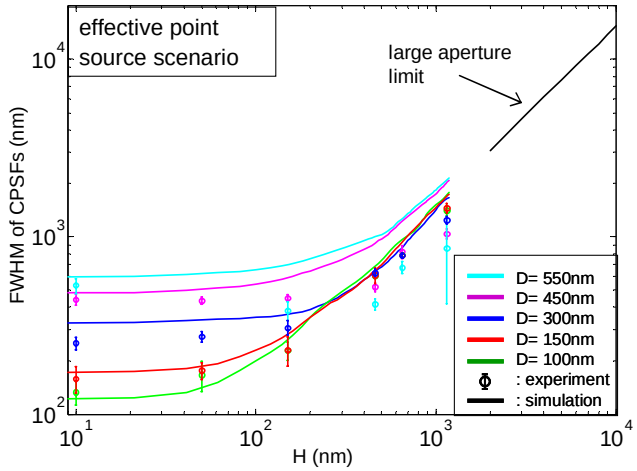

Fig. 8. (log-log scale): CPSF's FWHM *versus* the gap height (H) for a range of aperture sizes (effective point source scenario). The lines represent simulation results and the circles represent experimental data. Line sources of all three orientations were considered - the light source is modeled as an effective isotropic point source. Black line: the far field trend of large apertures (FWHM ~ 1.53 H). The collection N.A. for the transmission is effectively unity.

Table 1. Depth of field (DOF) of the subwavelength apertures

	D = 100 nm	D = 150 nm	D = 300 nm	D = 450 nm	D = 550 nm
DOF (Sim.)	130 nm	190 nm	440 nm	500 nm	610 nm

Note: Sim. : simulation. The simulation results shown in Fig. 8 were used to calculate the DOFs.

#74321 - $15.00 USD Received 22 August 2006; revised 18 October 2006; accepted 20 October 2006

The behavior of the CPSFs' width at large H values deserves some discussion. For large H, the light field incident on the aperture simplifies to a plane wave propagating along the direction from the light source to the aperture. This far field simplification allows us to analytically derive the CPSF behaviors for very large apertures. In the large aperture limit, the width of the CPSF will vary linearly with the point source height. The following paragraphs derive the exact relationship.

The transmission areas of very large apertures are the same as their physical areas. Therefore, the total transmission (*T*) through a large aperture is given by the surface integral of the incident Poynting vector field over the area of the aperture. In the far field limit, the treatment of the incident light field as a plane wave simplifies the integration to a product of the magnitude of the Poynting vector normal to the aperture ($S_\perp$), and the area of aperture (*A*):

$$T = S_\perp \cdot A = S(x,H)\cos(\theta)\cdot A = S(x,H)A\sqrt{\frac{H^2}{x^2+H^2}} \propto \frac{A}{x^2+H^2}\sqrt{\frac{H^2}{x^2+H^2}} \qquad (2)$$

where $S(x, H)$ is the average energy density above the open area of the aperture from a point source at height H and lateral displacement of x between the point source and the aperture; θ is the incident angle with $\theta=0$ representing normal incidence. The proportionality relationship is derived by noting that the light energy density is inversely proportional to the square of the distance between the source and the aperture. The profile of the aperture's CPSF is given by the expression in Eq. 2, and as such the FWHM of the resulting CPSF is equal to:

$$FWHM = 2\sqrt{2^{2/3}-1}\cdot H \approx 1.53H \qquad (3)$$

It is clear from Fig. 8 that all of the CPSFs' FWHM trends taper into a proportionality relationship with the source height (H). More specifically, the relationship is linear in nature. The large aperture limit trend given by Eq. (3) is plotted in Fig. 8 for comparison. While we expect the simulation results for the larger apertures to show convergence to this trend, it turns out that all of the simulation curves show fair convergence to this trend. This convergence suggests that aperture size has weak impact on the CPSF in the far field limit. At present, we do not have a good explanation for this behavior.

Finally, we will like to point out that the PSF behavior in the far field limit for very large apertures in type-I ABID configuration (see Fig. 1(a)) is very different. In this case, an incident planar illumination of wavelength (λ) on the input side of the aperture of size D will result in a well characterized diffraction pattern on the output side. In the far field regime, Fraunhofer diffraction calculation is valid. Based on this calculation, the diffraction pattern is described by Airy's disk [23]. Therefore, FWHM of the diffraction profile (i.e. PSF) is:

$$FWHM = 1.03\times\frac{\lambda}{D}\cdot H \qquad (4)$$

Unlike the CPSF for large aperture type-II ABIDs, the width of the PSF for large aperture type-I ABIDs is dependent on the illumination's wavelength, aperture size and the height of the plane of interest. This difference can be attributed to the fact that the two optical geometries are not optical complements for the reason pointed out in Section 1.

5.2 Impact of the numerical aperture (NA) of the collection optics on the observed CPSFs

As mentioned earlier, the collection optics' NA can impact on the observed CPSFs. Our experimental geometry enabled us to investigate the influence of the collection optics' NA in

#74321 - $15.00 USD Received 22 August 2006; revised 18 October 2006; accepted 20 October 2006

more details. This phenomenon can be further appreciated by taking a closer look at the following two scenarios:

a) Small apertures

First, consider a sufficiently small aperture such that it functions as a zero mode waveguide [1, 7]. In this case, the transmitted field pattern is simply the diffraction pattern associated with the aperture. The input light field pattern incident on the aperture has no effect on the transmission pattern. The independence of the output diffraction pattern on the input light field pattern extends approximately to apertures that are small enough to support only a small number of propagating modes. Fig. 9(a, b) show the results of our simulations of the transmission through a 300 nm wide aperture for a point source at height H =1.15μm and two different lateral displacements (x= 0 nm and x = -500 nm). It can be seen from our simulation that the strength of the transmission changes but the output diffraction pattern remains almost unchanged. This implies that the use of a high or low NA objective to collect the transmitted light should yield almost the same shape of a CPSF profile for the aperture. The use of a high NA objective merely enables the collection of more light from the output diffraction transmission.

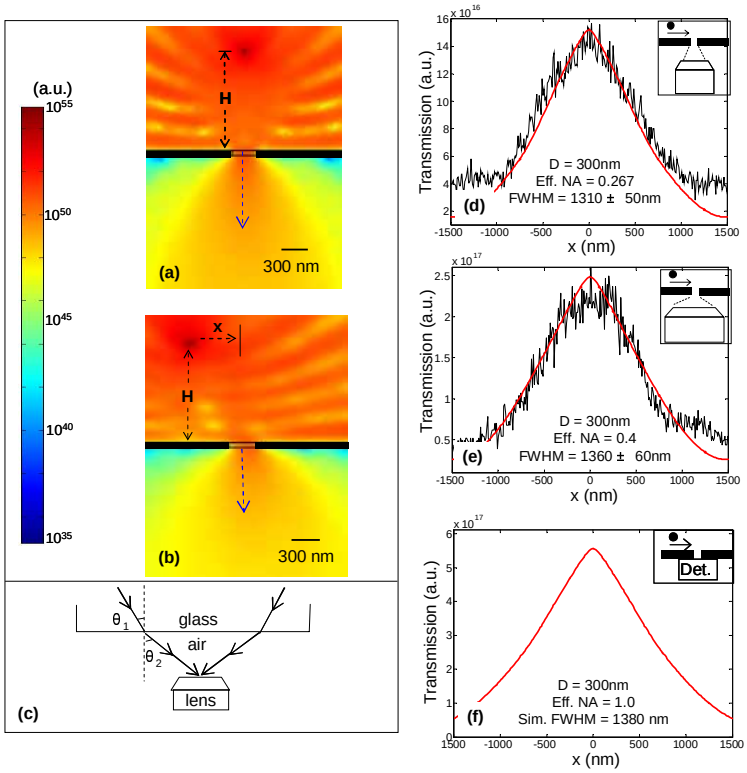

Fig. 9. (a), (b) 2D cross sectional plots of power flow, |S| for two different lateral displacements. The source lateral displacement is 0 in (a) and -500nm in (b). Aperture size is 300 nm; H= 1150 nm. (c) Light collection geometry in the experiment showing that the effective numerical aperture is reduced by the presence of the quartz wafer. (d) Plots of the CPSFs from experiment (black) and simulation (red dashed). Effective NA =0.267. H= 1150 nm. (e) Corresponding plots in the case where effective NA = 0.4. (f) Simulation CPSF curve with a perfect collection NA, i.e. NA=1.0. (Note that FWHMs indicated in figure (d) and (e) are obtained from experimental results. All the experimental FWHMs are summarized in Table 2.)

We performed an experiment with a 300 nm aperture to verify this prediction. The point source was scanned at a height of 1.15 μm above the aperture. Two objectives (NA = 0.6 and

#74321 - $15.00 USD Received 22 August 2006; revised 18 October 2006; accepted 20 October 2006

NA = 0.4) were used. Due to the intervening free space between the glass substrate and the collection optics, the effective collection NA is lower than the cited objective value. (See Fig 9(c) for an illustration of this consideration.) The effective NA of these two objectives is 0.4 and 0.267, respectively.

The measured CPSFs are plotted in Fig 9(d, e). As can be seen from the figures, our simulation results agree well with our experimental findings. The measured signal associated with the NA =0.4 setup (Fig. 9d) was lower than that for the NA = 0.6 setup (Fig. 9e); this is consistent with the fact that the lower NA system will collect less light from the diffracted transmission. For comparison, we also plotted the simulation result for the case where the collection NA = 1.0 (all the light is collected) in Fig. 9(f). In Fig. 9(d-f), the FWHMs of the two experimentally measured CPSFs match up well with the simulation result for the case where the NA is unity (5% and 1.4% difference, respectively). This illustrates the relative insensitivity of the measured CPSFs on the collection optic's NA for small apertures.

b) Large apertures

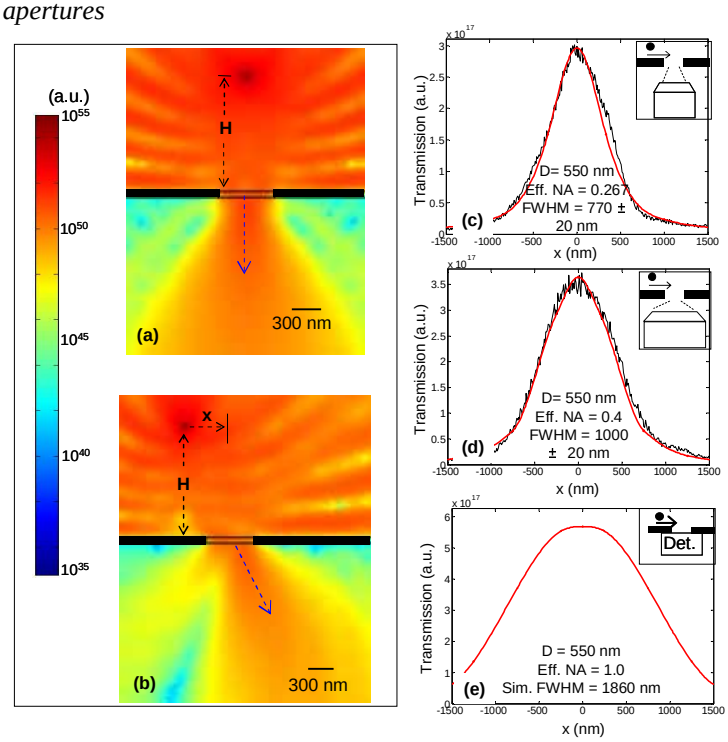

Fig. 10. (a), (b) 2D cross sectional plots of power flow, |S| for two different lateral displacements: 0 nm in (a) and -500nm in (b). Aperture size is 300 nm; H= 1150 nm. (c) Plots of the CPSFs from experiment (black) and simulation (red dashed). Effective NA= 0.267. H= 1150 nm. (d) Corresponding plots in the case where effective NA = 0.4. (e) Simulation CPSF curve with a perfect collection NA, i.e. NA=1.0. (Note that FWHMs indicated in figure (c) and (d) are obtained from experimental results. All the experimental FWHMs are summarized in Table 2.)

In contrast to small apertures, large apertures have a large number of propagating modes. In this case, the output diffraction pattern from the aperture depends strongly on the input light field profile and direction. We repeated the simulations corresponding to the results shown in Fig. 9(a, b) and substituted a 550 nm wide aperture in place of the 300 nm aperture. The results are shown in Fig 10(a, b). As can be seen in Fig 10(b), a laterally displaced point source (x= -500 nm) gives rise to a severely skewed output diffraction pattern.

#74321 - $15.00 USD Received 22 August 2006; revised 18 October 2006; accepted 20 October 2006

In this situation, the choice of the collection optics' NA has a significant impact on the observed CPSF. Explicitly, a small NA objective will fail to collect most of the transmitted light when the skew angle of the central diffraction lobe is larger than the collection angle of the objective. As such, a smaller collection NA system will give a narrower CPSF in comparison to a higher NA system.

This prediction is corroborated by an experiment with an aperture of size 550 nm. The experimental setup and parameters are similar to those for the above described experiment with the 300nm aperture. The measured CPSFs and the simulation profiles are plotted in Fig. 10(c, d). The experiment and simulation are again in good agreement. For comparison, we also plotted the simulation result for the case where the collection NA = 1.0 (all the light is collected) in Fig. 10 (e). The measured FWHMs of the CPSF for finite collection NA situations (FWHM = 770 nm for NA = 0.267, FWHM = 1000 nm for NA = 0.40) deviate very significantly from the simulation result for the ideal light collection case (NA = 1), where the FWHM is computed to be 1860 nm.

The results of Fig. 9 and Fig. 10 are summarized in Table 2. The finding suggests that it is possible to design type-II ABIDs to have a significantly reduced CPSF for large H values (i.e. far field), and consequently a longer DOF by restricting NA of the collection optics. This method is valid for relatively large apertures, but will have little impact on type-II ABIDs that use small apertures. However, the reduction of collection optics' NA will lead to decreased light collection efficiency and therefore reduced device's sensitivity.

Table 2: Summary of Fig. 9 and Fig. 10

Aperture Diameter	FWHM of the CPSF Effective NA= 0.267		FWHM of the CPSF Effective NA= 0.4		FWHM of the CPSF Perfect NA (NA= 1.0)
	Experiment	(Simulation)	Experiment	(Simulation)	(Simulation)
300 nm	1310 ± 50 nm	(1290 nm)	1360 ± 60 nm	(1350 nm)	(1380 nm)
550 nm	770 ± 20 nm	(710 nm)	1000 ± 20 nm	(970 nm)	(1860 nm)

Note: both the experiment data and the simulation data are acquired at a source height (H) equals to 1150 nm.

5.3 Comparison of the resolution of type-II ABIDs and a conventional microscope

The CPSF of the aperture is a direct correspondence to the PSF of a conventional microscope, as both of them can be used to characterize the ability of the specific imaging system to resolve objects. In this section, we will compare the resolution of type-II ABIDs to that of conventional microscopes. As mentioned in Section 4, the resolution limit of type-II ABIDs is reached only when the target is in close proximity to the aperture. The CPSF widens with an increasing target height (H). This behavior can be found in a conventional microscope as well – the associated PSF rapidly widens when a target moves away from the focal plane of a conventional microscope.

Fig. 11 shows the measured resolution limit for type-II ABIDs based on our simulation results for a range of aperture sizes. We chose the Sparrow's criterion for this determination for the reason stated in Section 2. We have also included the estimates based on our experimental data in the figure. However, due to the previously mentioned limitations in NSOM experiments, the estimates based on our experimental data tend to over estimate the resolution. The simulation results are more accurate and unbiased.

Within the range of our measurements, the result shows an approximately linear trend. A linear fit of the simulation data was added to the plot to indicate the trend, but we note that this linearity may not extend beyond the plotted range and is purely an empirical observation.

Within the range plotted in Fig. 11, the resolution limit of type-II ABIDs is consistently smaller than the physical size of the aperture. In fact, the resolution limit is approximately

#74321 - $15.00 USD Received 22 August 2006; revised 18 October 2006; accepted 20 October 2006

90% of the aperture's diameter based on our measurements. This empirical result is useful as a rule of thumb for estimating a type-II ABIDs' resolution when dealing with aperture diameter in the range of 100 nm to 1000 nm. We do not expect this trend to hold for aperture of all sizes. In the limiting case where the aperture is large (e.g. 100 μm), geometric optics is valid to analyze the system. The optical cross section of a large hole is the same as its physical area in the geometric optics regime. The CPSF at zero height should then be close to a top hat function with a width that is equal to the aperture's wide. In that situation, the resolution limit should be equal to the aperture's diameter.

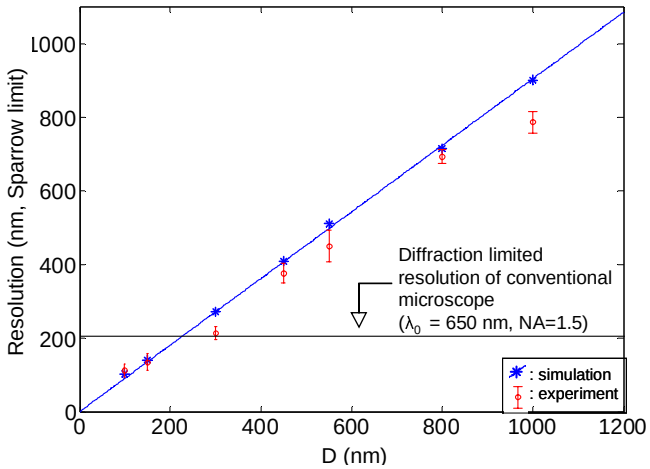

Fig. 11. Comparison of type II ABIDs with conventional microscopes. Blue asterisk: Near field resolution of type II ABIDs vs. D (simulation). Simulation assumed an effective isotropic point source. Blue dashed line: linear fit of the resolution limit of type II ABIDs. Red error bars: Near field resolution of type II ABIDs based on our experiment. Black dashed line: diffraction limited resolution of an ideal conventional microscope.

The dashed black line was also added to the plot to show the resolution limit (based on Sparrow's criterion) for an ideal diffraction limited conventional microscope with perfect NA. The medium's refractive index of 1.5 and a free-space wavelength of 650 nm were used in the calculation to match with the medium and illumination parameters in our subwavelength aperture study. Such a system has a resolution limit of about 200 nm. Based on the observed crossing point of this line with the simulation data fit, we can see that an aperture of size 225 nm can achieve the same resolution limit. Apertures that are smaller should therefore exceed the resolution limit of an ideal diffraction limited conventional microscope operating under the same wavelength and refractive index.

6. Conclusions

In summary, the light collection characteristics of subwavelength apertures with respect to point sources at varying heights and lateral displacements from the nanoaperture were systematically studied for the first time. We performed a set of NSOM-probe scanning experiments with apertures that range in size from 100 nm to 550 nm. We also ran a set of EM simulations based on the same geometry. The experimental results were used to verify our simulation results. We used our findings to gain a better understanding of type-II subwavelength aperture based imaging devices (ABIDs) – devices in which subwavelength apertures serve as light collection elements. We defined a parameter – collection mode point spread function (CPSF), which is similar to the point spread function for conventional microscopes, and used it to characterize the ABIDs.

Three significant findings were made in the study. 1) We found that, in the far field limit, the width of the CPSF increases linearly with source height (H). Our simulation results

#74321 - $15.00 USD Received 22 August 2006; revised 18 October 2006; accepted 20 October 2006

indicate that, for far field, the width of the CPSF is only weakly dependent on the size of the aperture. In the far field and large aperture limit, the width of the CPSF is independent of the aperture size. This implies that the CPSF behavior of type-II ABIDs is quite different from the PSF behavior of type-I ABIDs at those limits. 2) In experiment, the observed CPSF is dependent on the NA of the collection optics that gathers the transmission from the exit side of the aperture. Our study shows that the depth of field associated with apertures can be increased by restricting the NA of the collection optics. 3) We observed an empirical linear relationship between the resolution limit of type-II ABIDs and the aperture size for sizes ranging from 100 nm to 1000 nm. Our study shows that type-II ABIDs based on small nanoapertures can deliver ultrahigh resolution beyond the diffraction limit – a restriction on the resolution of an ideal conventional microscope.

Acknowledgments

We thank Zhenyu Li, Jaewoo Choi and James Adleman from Caltech, Dr. David Erickson from Cornell University, and Liang Feng from UCSD for helpful discussions. We are grateful to Dr. Scherer's group at Caltech and UCLA's Nanolab for their assistance in fabrication. We thank Caltech's Molecular Materials Resource Center for providing us with the NSOM system. This work was funded by DARPA Center for Optofluidic Integration (California Institute of Technology).

#74321 - $15.00 USD Received 22 August 2006; revised 18 October 2006; accepted 20 October 2006